Petroleum Science 23 (2026) 1371–1386

Contents lists available at ScienceDirect

Petroleum Science

journal homepage: www.keaipublishing.com/en/journals/petroleum-science

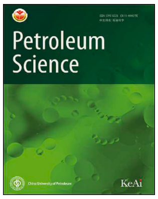

Original Paper

Investigation of fracture pressure and EOR mechanisms during fracturing flooding in low-permeability sandstone using CT and NMR

Lei Zhang [a,b], Hua-Peng Jing [a,b], Li-Yuan Dong [c], Gloire Imani [a,b], Dong-Yan Fan [a,b], Shuai-Shi Fu [a,b], Bilal Shams Memon [d], Yong-Fei Yang [a,b], Jun Yao [a,b], Hai Sun [a,b,*]

[a] *State Key Laboratory of Deep Oil and Gas, China University of Petroleum (East China), Qingdao, 266580, Shandong, China*
[b] *School of Petroleum Engineering, China University of Petroleum (East China), Qingdao, 266580, Shandong, China*
[c] *Engineering Technology Institute, CNOOC Energy Development Co., Ltd., Tianjin, 300457, China*
[d] *Department of Petroleum & Gas Engineering, Dawood University of Engineering & Technology Karachi, Karachi, Sindh, Pakistan*

ARTICLE INFO

Article history:
Received 10 November 2024
Received in revised form
3 January 2026
Accepted 6 January 2026
Available online 9 January 2026

Edited by Yan-Hua Sun

Keywords:
High water cut
Low permeability sandstone
Fracturing flooding
CT scanning
NMR
Reservoir modification
EOR

ABSTRACT

Fracturing flooding provides an effective approach to overcoming injection difficulties and enhancing oil recovery in high-water-cut, low-permeability sandstone reservoirs. Injecting fracturing-flooding fluids (FFFs) at high rates over short durations enables a coupled process of hydraulic fracturing and flooding, especially when the FFFs contain surfactants. In this study, two types of core experiments were conducted to elucidate the mechanisms of reservoir modification and residual oil mobilization during fracturing flooding. (1) Fracturing flooding combined with CT scanning: The effects of N_2 permeability (K_g) and FFF viscosity on fracture pressure (P_f) were investigated. Post-flooding CT scans of multiple cores were performed to visualize fracture propagation. (2) Fracturing flooding combined with NMR experiments: The recovery efficiencies of water-based and petroleum sulfonate (NPS)-based fracturing flooding were compared with conventional water flooding. The results showed a negative correlation between K_g and both P_f and the permeability enhancement factor (E_K), with E_K ranging from 1.61 to 0.43. Increasing FFF viscosity led to higher P_f values. The E_K first increased and then decreased, consistent with the fracture distribution observed in CT images. Moreover, NPS fracturing flooding exhibited superior enhanced oil recovery (EOR) performance compared with water fracturing flooding. The latter primarily improved recovery in small pores and mesopores, with recovery enhancement factors (E_R) of 0.44 and 0.36, respectively. In contrast, the NPS fracturing flooding achieved significant recovery improvements across all pore sizes, with E_R values in micropores and macropores approximately threefold and fifteenfold higher than those of water fracturing flooding. This study presents a novel investigation into the mechanisms of fracture propagation and enhanced oil recovery in fracturing flooding processes.

1. Introduction

With the continuous advancement of oilfield exploration and development technologies, low-permeability sandstone reservoirs have become an increasingly prominent target in global petroleum exploration and production. These reservoirs now represent one of the primary types in oilfield development (Jia et al., 2012). However, they are generally characterized by poor physical properties (Yin et al., 2020), low permeability (Pan et al., 2024), and complex pore structures (Wei et al., 2018; Zhong et al., 2020). After decades of exploitation, many low-permeability sandstone reservoirs have entered a high-water-cut stage (Guo et al., 2021), giving rise to new challenges. At this stage, water injection wells often exhibit poor injectivity and elevated injection pressures, occasionally resulting in injection refusal. Due to the sluggish diffusion of formation energy, production wells respond ineffectively to water injection, leading to production difficulties. Furthermore, prolonged high-pressure water injection frequently causes a rapid increase in water cut after breakthrough, followed by a sharp decline in both the liquid production index and the oil production index. Consequently, the overall recovery efficiency drops

---

[*] Corresponding author.
E-mail address: sunhai@upc.edu.cn (H. Sun).
Peer review under the responsibility of China University of Petroleum (Beijing).

https://doi.org/10.1016/j.petsci.2026.01.004

significantly (Li et al., 2018; Ma et al., 2021; Osiptsov, 2017). In view of these challenges, hydraulic fracturing has become an essential measure for sustaining and enhancing the productivity of such reservoirs.

Numerous researchers have conducted extensive experimental investigations on hydraulic fracturing, focusing primarily on fracture propagation and enhanced oil recovery (EOR). Table 1 summarizes several representative studies. Most of these works employ hydraulic fracturing with the primary goal of improving the conductivity of low-permeability reservoirs, including shale, coal seams, and tight sandstones. However, conventional hydraulic fracturing techniques (Aljawad et al., 2019) often cause significant formation damage and exhibit a relatively short effective lifespan. To address these limitations, the concept of fracturing flooding has been proposed. In this approach, the displacement agent simultaneously serves as the fracturing fluid, flowing along the newly created fracture pathways to rapidly invade the pore network. This process reduces prolonged fluid–rock contact while swiftly replenishing reservoir energy (He and Wang, 2018). It is important to emphasize that the mechanism of fracture propagation in fracturing flooding differs fundamentally from that in conventional hydraulic fracturing. In traditional fracturing, the objective is to minimize fluid loss and promote the continuous extension of fractures. Conversely, fracturing flooding intentionally facilitates fluid loss to enhance fluid penetration into the formation, thereby slowing fracture growth. Consequently, it is crucial to recharacterize and deepen our understanding of fracture propagation behavior and morphology within the framework of the fracturing flooding process.

Computed tomography (CT) scanning has long been a crucial technique for visualizing pore structures and conducting image analysis (Yerramilli et al., 2015), with extensive applications in petroleum engineering (Jing et al., 2024). By employing advanced optical instrumentation, CT scanning enables three-dimensional imaging of porous media (Cnudde et al., 2011; Liu et al., 2023). Continuous scanning facilitates differentiation between online and offline modes, while in-situ scanning can be performed for specialized samples. In recent years, CT scanning has become an indispensable method for characterizing the pore structures of various reservoir types, including low-permeability sandstone (Bai et al., 2013; Liu et al., 2017), carbonate rocks (Lian et al., 2020), and shale (Tiwari et al., 2013). When combined with reservoir damage experiments, CT scanning provides a powerful means of examining dynamic changes in pore structure (Liu et al., 2019; Ma and Chen, 2014; Shi et al., 2012). The integration of flow experiments with online CT scanning, coupled with advanced image-processing techniques, establishes a robust foundation for studying microscopic fluid behavior and its dynamic evolution under varying conditions (Ding et al., 2024), as well as for visualizing the oil–water displacement process (Feng et al., 2004). Numerous studies have utilized CT scanning to investigate fracture propagation during fracturing flooding (Liu et al., 2019; Ma et al., 2022; Nguyen et al., 2022; Yang et al., 2023c; Zhang et al., 2022). These studies revealed that radial planar fractures readily develop within the core following the implementation of fracturing flooding (Wei et al., 2018).

Nuclear magnetic resonance (NMR) is another widely applied technique for characterizing reservoir pore structures (Guo et al., 2020; Wang et al., 2017). In certain research areas, NMR can serve as an alternative or complement to CT scanning, such as in pore structure characterization (Lai et al., 2016; Wang et al., 2020), stress-sensitivity analysis (Gao et al., 2019), and imbibition simulation experiments (Cheng et al., 2018; Yang et al., 2023a). Two-dimensional NMR is particularly useful for distinguishing between movable oil and water phases (Bai et al., 2021). Because NMR provides information on pore size distribution and fluid

Table 1
Main findings on fracturing techniques in low-permeability reservoirs.

Experimental type	Material	Fluid	Main finding
Hydraulic fracturing	Coal	Water	The influence of different fracturing parameters on the generated fracture network was clarified (Li et al., 2013; Zhai et al., 2011).
	Coal	Water	The observed cracks primarily emanate from the original transverse cracks on the injection hole wall (Shi et al., 2016).
	Shale	Water, viscous oil	Viscous oil produces a single linear fracture, while water produces branching fractures (Bennour et al., 2015).
	Shale	Water, liquid CO_2 (L-CO_2)	Fractures induced by water are predominantly macro-fractures, whereas fractures induced by liquid CO_2 consist of both micro- and macro-fractures (Mu et al., 2021).
	Low permeability sandstone	Water	Dynamic observation of fluid–rock interaction and fracture network development (Ma et al., 2022).
	Low permeability sandstone	Supercritical CO_2 (SC-CO_2), slickwater	SC-CO_2 fracturing has been shown to exhibit a lower fracture pressure in comparison to slickwater fracturing (She et al., 2023).
	Shale–sandstone interbedded	Water	A significant vertical stress difference is essential for the successful formation of multi-layer hydraulic fractures (Yang et al., 2023b).
	Shale	SC-CO_2	Pre-injection of SC-CO_2 enhanced the plastic deformation behavior of shale, and its breakdown pressure was 16.6% lower than that of water (Zang et al., 2024).
	Tight sandstone	Water	Elevated temperature and horizontal stress differentials contribute to enhanced fracture propagation (Ju et al., 2025).
	Sandstone	Water	Stress shadow effect significantly influenced the fracture propagation path (Jiang et al., 2025).
	Sandstone	Sodium dodecyl sulfate	Higher surfactant concentrations enhance hydrophilicity (Wang et al., 2025).
	Low permeability sandstone	SC-CO_2, water	SC-CO_2 fracturing generates a more complex fracture morphology compared to water-based fracturing (Yang et al., 2025).
Fracturing flooding	Low permeability sandstone	Guar gum	The crack propagation process can be categorized into three distinct stages: elastic deformation, micro-fracture initiation, and unstable fracture (Sun et al., 2024).
	Low permeability sandstone	Guar gum, NPS	A larger energy deficit corresponds to a greater increase in the recovery efficiency (Liu et al., 2022).
	Tight sandstone	KCl	Radially extending vertical fracturing is generated during fracturing flooding (Zhang et al., 2022).
	Low permeability sandstone	Water, NPS	High-pressure drop adsorption enhances the oil recovery efficiency of FFFs (Wang et al., 2024).

properties, it serves as an effective tool for analyzing the distribution and utilization of residual oil after fracturing flooding. The method has been employed to examine residual oil behavior following surfactant-assisted fracturing flooding (Jiang et al., 2022), where a leftward shift in the T_2 peak was observed, accompanied by enhanced oil utilization in sub-mesopore regions. Furthermore, some studies have combined NMR with mercury intrusion porosimetry to investigate pore structure evolution and physical parameter changes in cores (Zhang et al., 2022). Their results showed that after fracturing flooding, the average pore radius increased by 3%–8%, porosity rose by 2%–5%, and permeability improved by more than threefold, indicating that fracturing flooding significantly modifies the pore structure of the core.

Table 1 summarizes the principal contributions of conventional hydraulic fracturing and fracturing flooding approaches and highlights their main findings. While these studies have advanced our understanding of fracture behavior under fracturing flooding conditions, several important issues remain unresolved. Two topics in particular warrant further investigation. First, the influence of fracturing flooding fluid (FFF) viscosity on fracture pressure (P_f) and fracture propagation dynamics is not yet fully characterized (in this context, “viscosity” denotes the viscosity of FFFs). Second, the extent to which fracturing flooding (whether water-based or surfactant-based) enhances reservoir seepage capacity, alters fracture distribution, and mobilizes residual oil across different pore size scales remains unclear. Both issues are central to optimizing field applications and provide practical metrics for evaluating the effectiveness of fracturing flooding treatments.

Consequently, this study investigates these mechanisms using a combination of CT scanning and NMR analyses. N_2 permeability (K_g) and fluid viscosity were selected as variables in flow rate-pressure difference experiments. The fracture pressure was identified from the inflection point of the recorded data to evaluate the effects of K_g and viscosity on P_f. Subsequent CT scanning was conducted to obtain post-flooding core images for comparison with the experimental results. NMR experiments were performed to assess the recovery performance of conventional water flooding, water-based fracturing flooding, and petroleum sulfonate (NPS) fracturing flooding. The influence of varying displacement stages and the residual oil distribution after fracturing flooding with different FFFs was analyzed. T_2 spectrum analysis was used to identify the mobilized oil-bearing pores and to quantify the degree of EOR across different pore size ranges.

The experimental results revealed that P_f did not exhibit a strict positive correlation with fluid viscosity, a finding further supported by the CT imaging observations. Moreover, NPS fracturing flooding achieved superior EOR performance across a wider range of pore sizes and to a greater extent than water-based.

2. Experiment and methodology

2.1. Materials

2.1.1. Core sample

This study utilized low-permeability sandstone cores with a diameter of 2.5 cm obtained from a specific reservoir block, as shown in Fig. 1(a). The fundamental physical properties of the cores were evaluated and are presented in Fig. 1(b). As depicted in Fig. 1(c), permeability mapping was used to visually display the spatial variability of permeability within the core set. A total of twelve cores were divided into three groups. Set #1, consisting of six cores, was used to investigate the effect of K_g on fracturing flooding. The K_g values of Set #1 ranged from 5.22×10^{-3} to 20.40×10^{-3} μm^2, with porosity values between 4.5% and 17.3%.

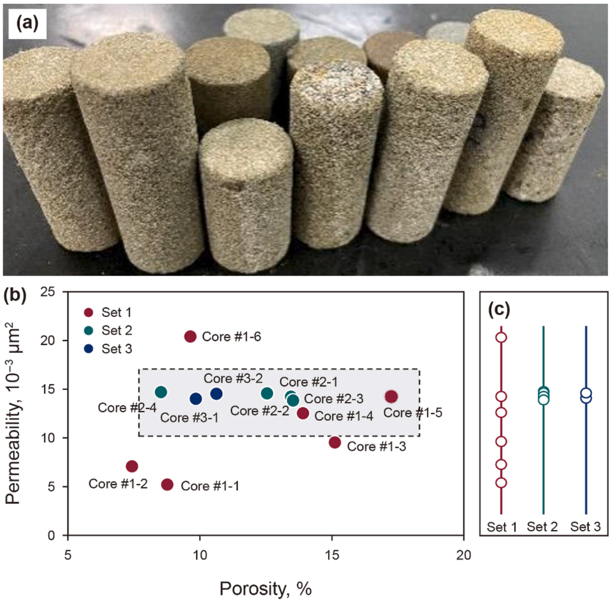

Fig. 1. Core samples. (**a**) Photographs of all core samples; (**b**) basic physical properties, including porosity and permeability; (**c**) permeability distribution map, with coordinates corresponding to those in (b). The cores enclosed by the dashed box were selected for parallel comparison across different experimental conditions.

Set #2, comprising four cores, was designed to evaluate the effect of fluid viscosity while maintaining comparable K_g values across the samples. Core #1-5, which exhibited permeability similar to that of Set #2, is used for comparative analyses across multiple experiments. These ten cores collectively formed the experimental basis for the reservoir modification study. Set #3, consisting of two cores, was used for integrated fracturing flooding and NMR experiments to examine EOR performance and the mobilization behavior of residual oil across different pore size ranges.

2.1.2. Preparation and properties of fluids

The viscosities of oil and water in the target reservoir, as determined from field data, are 2.15 and 0.39 mPa·s, respectively, yielding an oil–water viscosity ratio of 5.615. The viscosity of the prepared simulated formation water (hereafter referred to as water) was measured to be 0.41 mPa·s. To maintain consistency with the reservoir oil–water viscosity ratio, a simulated formation oil (hereafter referred to as oil) was formulated by blending ground degassed crude oil (obtained from the same oilfield) with kerosene in varying proportions. The viscosity of ground degassed crude oil at the experimental temperature of 70 °C was 10.736 mPa·s. The masses of kerosene and ground degassed crude oil are denoted as m_k and m_{gdco}, respectively. Table 2 lists the viscosities of mixtures with different m_k/m_{gdco} ratios. Based on the fitting curve shown in Fig. 2, the mass ratio corresponding to a viscosity of 2.30 mPa·s was determined to be 61.44. The oil was subsequently prepared according to this ratio for the following experiments. The density of the prepared oil was measured to be 0.81 g/cm^3.

Table 2
Viscosity of oil at different mass ratios.

m_{gdco}, g	m_k, g	m_k/m_{gdco}, %	Viscosity (70 °C), mPa·s
30.000	0	0	10.736
29.587	2.534	8.57	9.560
31.248	12.539	40.13	4.999
28.993	14.504	50.03	4.035
30.158	19.177	63.59	2.005

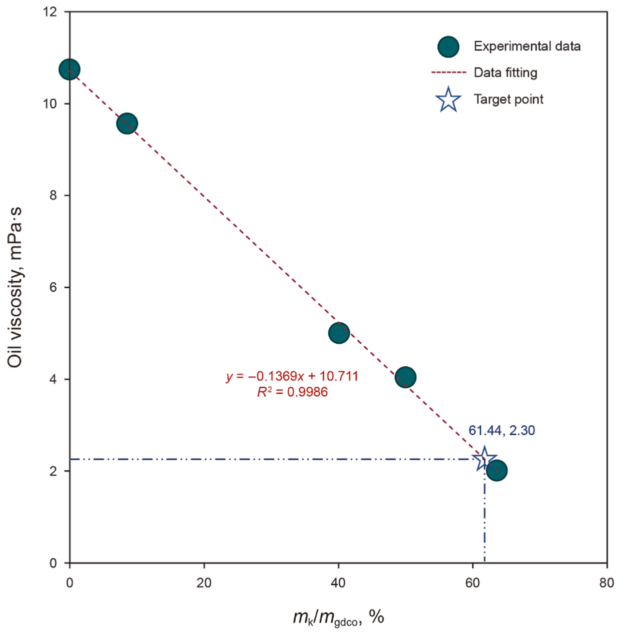

Fig. 2. Oil viscosity as a function of mass ratio of kerosene to ground degassed crude oil, with fitted calibration curve.

NPS exhibits excellent performance and is often combined with other surfactants to formulate composite surfactant flooding agents. Compared with many other surfactants, NPS shows superior stability in aqueous solutions (Ren et al., 2021), maintaining a strong ability to reduce interfacial tension even under high pressure conditions. Numerous studies have confirmed the effectiveness of NPS in enhancing oil recovery (Jiang et al., 2022; Li et al., 2023; Liao et al., 2017; Liu et al., 2022; Negin et al., 2017; Sun et al., 2020) compared the performance of NPS, guar gum, and formation water in fracturing flooding experiments and found that NPS achieved the largest swept volume, the highest oil-washing efficiency, and the greatest overall recovery. In addition, hydrolyzed polyacrylamide (HPAM) has been widely recognized as an effective polymer for oil displacement (Chen et al., 2023; Dai et al., 2024; Seright and Wang, 2023), with favorable stability for laboratory experiments. The present study does not aim to compare various types of FFFs but rather to evaluate the EOR potential of specific surfactants and clarify the differences between surfactant-based and formation water fracturing flooding. Therefore, water, HPAM, and NPS were selected as the representative FFFs based on their proven efficacy in prior research and field applications (Wang et al., 2024). Four HPAM solutions were prepared with viscosities of 5.0, 10.0, 19.0, and 33.9 mPa·s, respectively. A 0.3 % NPS solution was also prepared and filtered to remove impurities, yielding a viscosity of 3.3 mPa·s. The interfacial tensions of the three FFFs were measured, and the results are listed in Table 3. The same simulated oil prepared earlier was used as the test oil. To suppress the hydrogen signal during NMR measurements, all FFFs were prepared with a 20% $MnCl_2$ solution, which exhibits an interfacial tension similar to that of water.

Table 3
Interfacial tension results of FFFs.

FFF Type	Mass concentration, %	Oil–water interfacial tension, mN/m
Water	–	11.85
NPS	0.3	0.036
$MnCl_2$	20.0	10.59

2.2. Experimental setup and procedure

Two distinct experimental designs were developed: fracturing flooding combined with CT scanning experiments employed water and HPAM, while fracturing flooding combined with NMR experiments utilized water and NPS. As illustrated in Fig. 3(a), the relationship between the two experimental components is evident. The rationale behind this design lies in the fact that the P_f serves as the most direct indicator of the fracturing flooding simulation, representing the critical pressure at which rock failure occurs. Accordingly, the first experiment investigates how P_f correlates with both rock and fluid properties. Rock properties are expressed in terms of core permeability (a macroscopic characteristic governing fluid migration), whereas porosity primarily reflects storage capacity. Fluid properties are represented by viscosity, adjusted through varying HPAM concentrations. The second experiment focuses on evaluating the EOR performance of fracturing flooding. Two cores with comparable permeability are employed, ensuring that their injection pressures are identical and maintained near the P_f values determined from the first experiment. Consequently, it is reasonable to compare the EOR performance of different FFFs under these controlled conditions.

A standardized experimental procedure was established, as shown in Fig. 3(b). This procedure applies to both experimental types, differing only in the fluids used within the constant temperature apparatus and in the subsequent CT or NMR analyses. The high-temperature, high-pressure intermediate container stores the FFFs and connects to a high-precision ISCO pump that maintains the injection pressure. The high-pressure core holder sustains the required confining conditions and is linked to both a digital pressure gauge and the intermediate container via a three-way valve, with the outlet connected to a measuring unit. The maximum confining pressure is 60 MPa, and the operating temperature is 70 °C.

It is noteworthy that high-pressure saturated water (without hydrogen signal shielding) was employed for initial saturation, and all subsequent stages adopted injection saturation. The rationale is twofold:

(1) The rock's pore system is intricate, containing numerous fine pores and throats. The high-pressure saturation method uses a pressure gradient to rapidly drive water into these micro-pores and complex networks, achieving full and uniform saturation in a shorter time.
(2) The subsequent injection saturation more accurately replicates reservoir conditions. In subsurface environments, oil migrates through rock pores via seepage. Injection saturation mimics this process by allowing oil to penetrate and occupy the pore space in a realistic manner, thereby aligning laboratory simulations with the reservoir's actual physical state.

2.2.1. Fracturing flooding combined with CT scanning experiments

The cores from Sets #1 and #2 were utilized for the fracturing flooding experiments combined with CT scanning. The experimental temperature was maintained at 70 °C, and the confining pressure was consistently set 3 MPa higher than the inlet pressure. The employed FFFs were water and HPAM solutions. The experimental design was as follows: cores from Set #1 were subjected to fracturing flooding by injecting water, whereas cores from Set #2 were injected with HPAM solutions of varying viscosities. This setup aimed to investigate the effects of K_g and viscosity on P_f, examine fracture propagation behavior after fracturing flooding, and identify the key controlling factors. The specific experimental procedures were as follows:

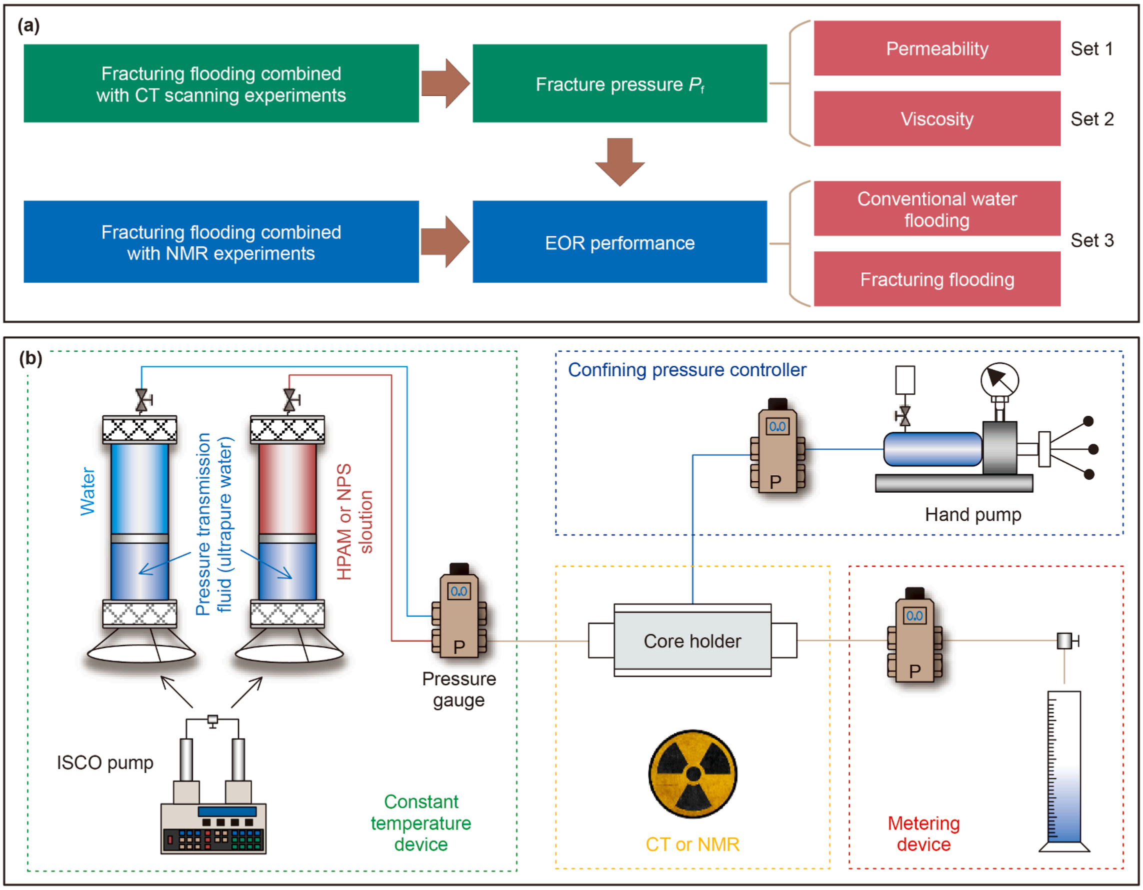

Fig. 3. Experimental design and interrelation of the two components. (**a**) Schematic illustrating the relationship between the two experimental parts; (**b**) layout of the experimental apparatus.

(1) The dry cores were placed under vacuum for 48 h at −0.1 MPa, gradually reaching a final pressure of 0.0098 MPa, and then saturated with water at 10 MPa for 72 h.
(2) The saturated cores were placed in the core holder, where the net confining pressure and temperature were adjusted. FFFs were injected at a constant rate using an injection pump, with the outlet connected to a measuring device. The inlet and outlet pressures were recorded every 10 min. When the pressure variation between two consecutive readings was less than 0.01% and the injected volume exceeded 10 pore volume (PV), the pressure readings were considered stable. The pressure differential and flow rate across the core were continuously recorded.
(3) The injection rate was then gradually increased until a sudden pressure drop occurred, indicating the initiation of fractures within the core. This inflection point corresponds to the P_f.
(4) After fracturing flooding, the cores were subjected to CT scanning for post-experimental analysis.

2.2.2. *Fracturing flooding combined with NMR experiments*

Cores from Set #3 were subjected to fracturing flooding combined with NMR experiments, in which water and NPS served as the FFFs. The experimental procedure, illustrated in Fig. 4, was conducted as follows:

(1) The cores were placed under vacuum for 48 h at −0.1 MPa, gradually reaching a final pressure of 0.0098 MPa. They were then saturated with water at 10 MPa for 72 h.
(2) The saturated cores were placed in the core holder for NMR testing to measure the T_2 spectrum. Afterwards, the cores were displaced with water containing 20% $MnCl_2$ solution for 30 PV.
(3) Oil was injected at a constant rate of 0.001 mL/min until no water was produced at the outlet, followed by an increased rate of 0.1 mL/min. A total of 15 PV was injected at each rate. After the injection, the system was depressurized and aged at a constant temperature for 24 h. Subsequently, the T_2 spectrum under oil-saturated conditions was measured via NMR.
(4) Water flooding was simulated by applying confining pressure and injecting water containing 20% $MnCl_2$ at a flow rate of 0.1 mL/min for oil displacement until no oil was produced at the outlet. The process was then halted, and NMR testing was conducted to acquire the T_2 spectrum.
(5) The FFFs containing 20% $MnCl_2$ were injected at a rate of 15 mL/min (under pressure slightly below P_f) for oil displacement until no oil was produced at the outlet.
(6) The inlet and outlet valves were then closed to simulate the well shut-in process, allowing oil–water redistribution for 24 h. Afterwards, continuous water injection was resumed

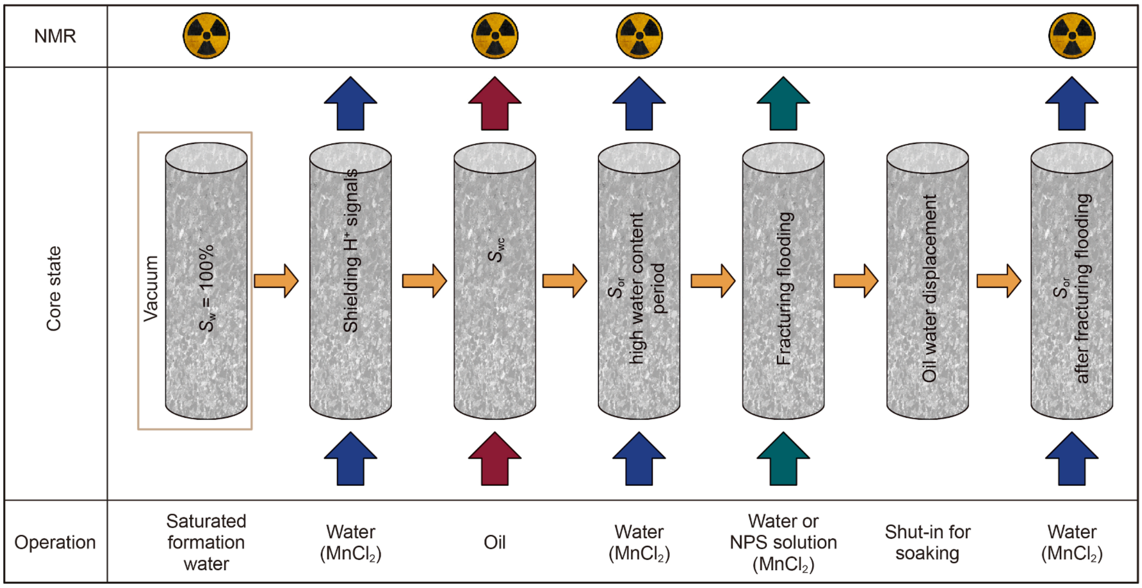

Fig. 4. Flow chart of fracturing flooding combined with NMR experiments.

until no additional oil was produced at the outlet. The produced fluid and oil volumes were recorded, and a final NMR test was performed to obtain the T_2 spectrum.

3. Results and discussion

3.1. Fracture pressure

3.1.1. Core permeability

The objective of this section is to determine the P_f of cores exhibiting different initial permeabilities (K_g). To achieve this, flow rate–pressure difference measurements were conducted. The inflection point on each flow rate–pressure difference curve signifies a change in the core permeability, which characterizes the onset of fracturing. The corresponding pressure value at this inflection point is used to establish the quantitative relationship between P_f and K_g.

Fig. 5 presents the flow rate–pressure difference curves for the cores from Set #1. The overall leftward shift of the curves demonstrates that as the permeability increases, the P_f decreases, and the fracturing flow rate increases. Each curve can be divided into three distinct flow stages:

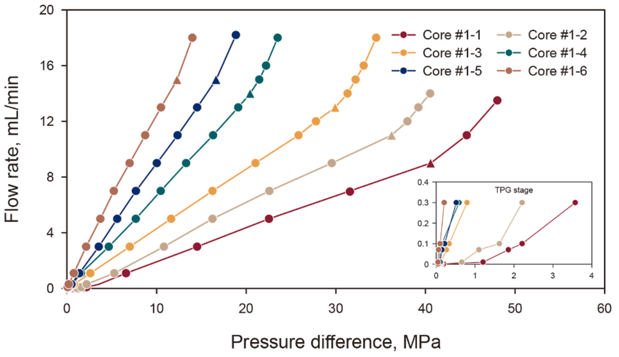

Fig. 5. Flow rate–pressure difference curves of Set #1.

(1) Threshold pressure gradient (TPG) stage: The small pore sizes typical of low-permeability reservoirs lead to strong capillary effects that hinder water injection, resulting in a gradual increase in pressure.

(2) Darcy flow stage: As injection proceeds, the pressure exerted on the pore throats rises sharply until it reaches P_f, at which point the core fractures.

(3) Post-fracture stage: Once the injection flow rate surpasses a certain threshold, the core undergoes fracturing due to the high flow rate and pressure, evidenced by a steeper slope on the curve that reflects enhanced permeability.

A noteworthy phenomenon was observed during the TPG stage. As the K_g increases, the TPG stage becomes progressively shorter. For instance, the first two data points of core #1-6 nearly overlap, indicating an extremely brief TPG stage. The corresponding pressure difference between these two points is 0.001 MPa, whereas that of core #1-1 is 1.664 MPa, as shown in the inset of Fig. 5.

The relationship between K_g and P_f can thus be summarized as follows: cores with higher permeability exhibit smaller pressure differences when reaching steady-state flow at the same injection rate. This can be attributed to the enhanced connectivity and lower seepage resistance in high-permeability cores, which favour the formation of dominant flow channels and facilitate stability at lower pressure differences. A subsequent quantitative analysis of the K_g–P_f correlation was conducted using these experimental data.

Table 4 summarizes the measured P_f and their corresponding flow rates for the six cores, while Fig. 6 illustrates the relationship between P_f and K_g. The results indicate that K_g exerts a significant influence on P_f, with lower K_g leading to higher P_f values. This relationship arises because a smaller K_g reflects a denser pore structure, poorer pore connectivity, and greater rock strength, which together necessitate higher stress to induce fracturing. Consequently, cores with lower permeability exhibit higher fracture pressures. Understanding this trend is essential for interpreting the fracturing behavior of low-permeability sandstone and elucidating how rock permeability governs fracture initiation and propagation during fracturing flooding.

Table 4
P_f and corresponding flow rate of Set #1.

Core No.	Permeability K_g, 10^{-3} μm^2	Flow rate, mL/min	Fracture pressure P_f, MPa
#1-1	5.219	9	40.59
#1-2	7.091	11	36.23
#1-3	9.524	13	29.94
#1-4	12.531	14	20.45
#1-5	14.250	15	16.65
#1-6	20.400	15	12.28

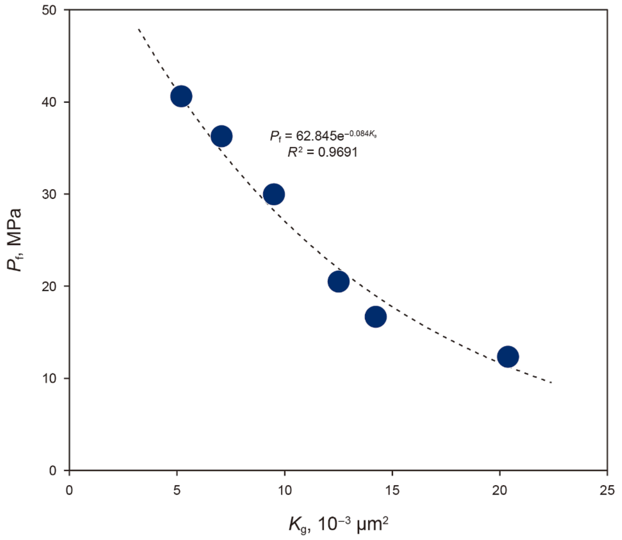

Fig. 6. Fitted curve of P_f versus K_g.

The relationship between P_f and K_g was fitted simultaneously, as shown in Eq. (1).

$$P_f = 62.845e^{-0.084K_g} \tag{1}$$

where P_f represents the fracture pressure, MPa; K_g denotes the permeability, 10^{-3} μm^2.

Although the coefficients in Eq. (1) are not universally applicable across all reservoirs, the results clearly indicate a negative exponential relationship between P_f and K_g. This trend suggests that as the reservoir permeability increases, the rate of decline in P_f diminishes rapidly.

This relationship offers a practical means of assessing whether fracturing flooding is warranted for a given sandstone reservoir. Specifically, when the permeability is high, the fracturing flooding process is characterized by a high flow rate and a low fracture pressure, which together lead to a substantial increase in the consumption and cost of fracturing flooding fluids. Therefore, from a theoretical standpoint, fracturing flooding technology is better suited to low-permeability reservoirs, where, for the same injected fluid volume, the enhancement in permeability is significantly greater than that observed in high-permeability formations.

3.1.2. Viscosity of FFFs

The experiment was conducted to investigate the behavior of cores with identical K_g under the injection of FFFs of varying viscosities. By analysing the pressure values corresponding to the inflection points on the flow rate–pressure difference curves, the relationship between P_f and viscosity was derived. This analysis provides insight into the mechanisms by which fluid viscosity influences the core fracturing process, offering valuable guidance for optimizing the selection and injection parameters of FFFs.

It was observed that the porosity of all cores in Set #2 varied slightly, with core #2-4 exhibiting a lower porosity than the others. However, this variation does not significantly affect the relationship between viscosity and fracture pressure, as the conductivity of fluid flow is primarily governed by permeability, and porosity data were not quantitatively analyzed in this context.

Fig. 7 presents the results of injecting fluids of different viscosities into the cores from Set #2. Similar to the previous experiments, all four cores exhibited a TPG stage. Owing to the short duration of this stage, the data points for cores #2-2 and #2-4 overlap in Fig. 7(b) and (d), respectively. Given the minimal variation in permeability among Set #2 cores and the results of the preceding experiments, it can be inferred that the TPG stage is not readily distinguishable, ranging from a minimum of 0.02 MPa (Fig. 7(d)) to a maximum of 0.6 MPa (Fig. 7(a)), and showing no clear correlation with fluid viscosity.

A comparison of the vertical coordinates of the subplots indicates a pronounced decrease in flow rate at P_f, dropping from 15 mL/min for core #2-1 to 0.3 mL/min for core #2-4, representing a nearly 50-fold reduction. This finding suggests that high viscosity significantly impedes flow capacity.

Table 5 summarizes the P_f and corresponding flow rates for cores #2-1 to #2-4 and core #1-5, while Fig. 8 demonstrates that P_f increases with increasing viscosity, further substantiating this trend.

Furthermore, the relationship between η and P_f was determined as follows:

$$P_f = 4.9718\ln(\eta) + 16.862 \tag{2}$$

where η represents the viscosity of FFFs, mPa·s.

Our results reveal that P_f increases logarithmically with viscosity. This implies that when the reservoir properties are relatively similar, the rate of P_f growth slows after reaching a certain viscosity level, even if viscosity continues to rise. In other words, there exists an optimal viscosity value that maintains a relatively high P_f while controlling economic costs. A higher P_f leads to greater FFFs loss, which is considered a desirable outcome. Therefore, viscosity optimization is essential. As previously mentioned, it is crucial to balance viscosity, flow rate, P_f, and reservoir permeability to achieve optimal economic and production performance. Further investigations are necessary to determine the most effective implementation strategies and development approaches.

3.1.3. Post-fracturing flooding

To better elucidate the changes in core permeability following fracturing flooding and the factors influencing this process, we introduce the permeability enhancement factor (E_K), which quantifies the variation in core permeability before and after fracturing flooding. The principle is derived from Darcy's law; however, since the fluid viscosity, core length, and cross-sectional area remain constant, permeability is directly proportional to the slope of the flow rate–pressure difference curve, expressed as the ratio of the experimental flow rate to the experimental pressure

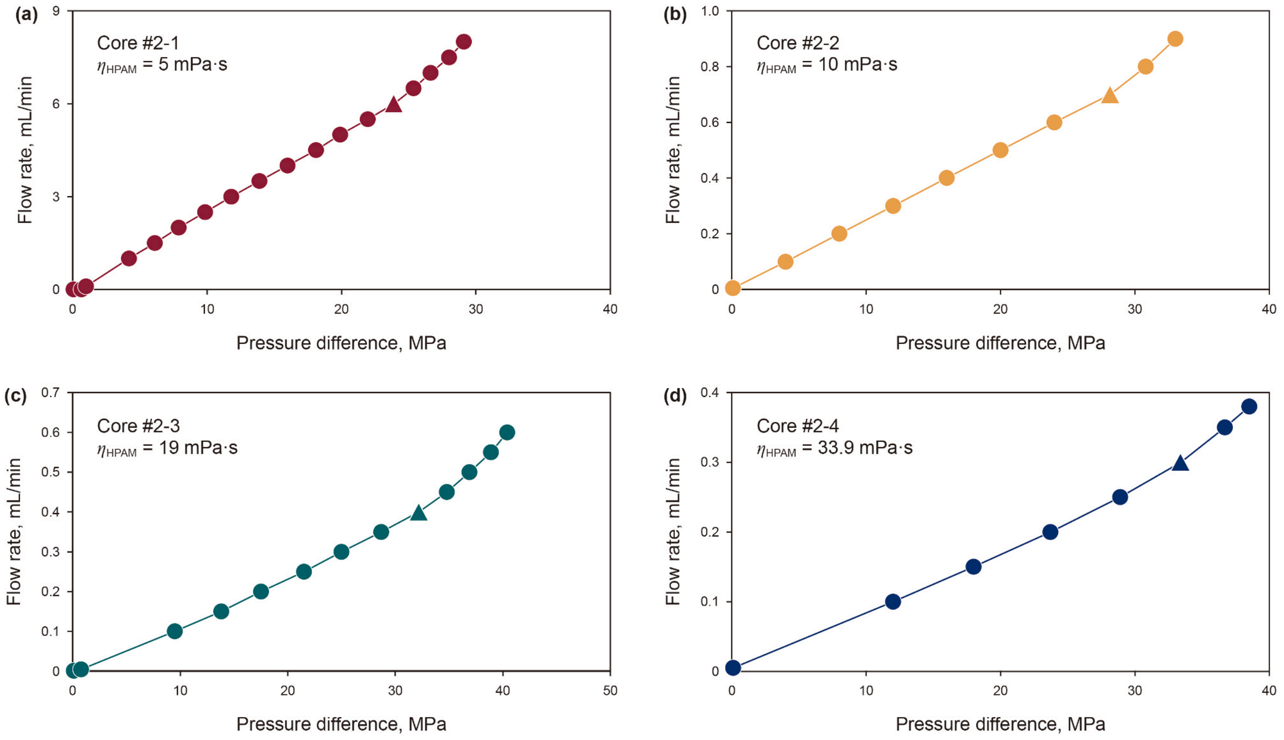

Fig. 7. Flow rate–pressure difference curves of Set #2. (**a**)–(**d**) correspond to cores #2-1 through #2-4, with HPAM viscosities of 5, 10, 19, and 33.9 mPa·s, respectively.

Table 5
P_f and corresponding flow rate of Set #2.

Core No.	Viscosity η, mPa·s	Flow rate, mL/min	Fracture pressure P_f, MPa
#1-5	1.0	15.0	16.65
#2-1	5.0	6.0	23.90
#2-2	10.0	0.7	28.15
#2-3	19.0	0.4	32.19
#2-4	33.9	0.3	33.40

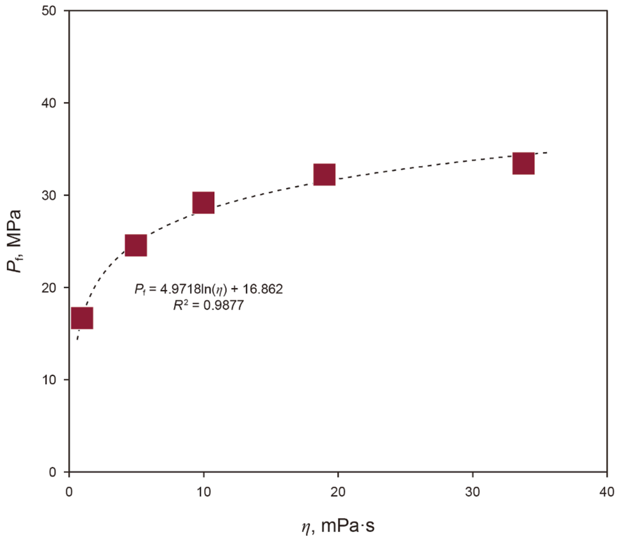

Fig. 8. Fitted curve of P_f and η.

difference. The slope is determined using data obtained after the points corresponding to the TPG stage and the fracture pressure point are excluded, unless only one data point remains after the fracture point, because a brief period is required to ensure stable pressure transmission when the flow capacity changes before and after fracturing.

$$k = \frac{Q\mu L}{A\Delta P} \quad \rightarrow \quad k \propto \frac{Q}{\Delta P} \tag{3}$$

$$E_K = \frac{k_2 - k_1}{k_1} \tag{4}$$

$$\begin{cases} k_1 = \dfrac{Q_1}{\Delta P_1} \\ k_2 = \dfrac{Q_2}{\Delta P_2} \end{cases} \tag{5}$$

The left-hand side of Eq. (3) represents Darcy's law, while the right-hand side provides the simplified form used in this study. In Eq. (4), E_K denotes the permeability enhancement factor, dimensionless. Here, k_1, Q_1, and ΔP_1 correspond to the permeability, flow rate, and pressure difference before core fracturing, respectively, whereas k_2, Q_2, and ΔP_2 correspond to those after core fracturing.

To calculate E_K after fracturing flooding, data from the previous experiments were processed, and correlation curves between E_K and both K_g and η were established. Fig. 9 presents the variation of E_K with K_g under water flooding at a uniform viscosity. A clear negative correlation was observed between the two parameters, indicating that E_K decreases as K_g increases. This trend can be explained as follows: K_g reflects the intrinsic permeability characteristics of the core. A higher K_g signifies larger pore throats and better pore connectivity, which reduces the relative contribution of newly formed fractures to overall permeability. In contrast, cores with lower K_g exhibit poor intrinsic connectivity; thus, the fractures generated during fracturing flooding become dominant flow pathways, significantly enhancing permeability. The maximum observed E_K value was 1.61, implying that post-

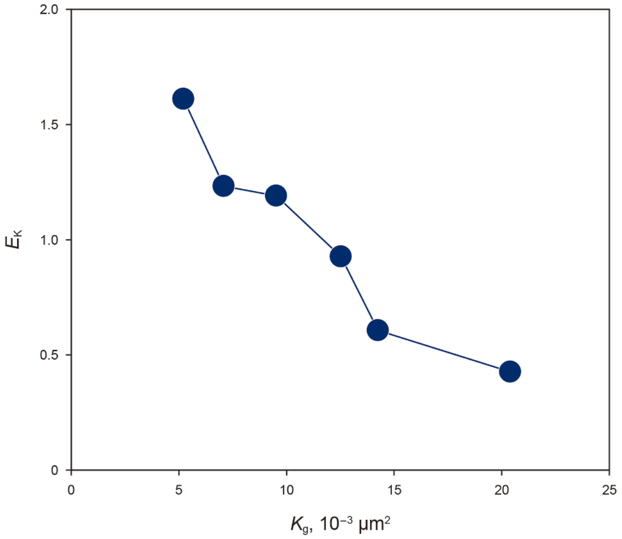

Fig. 9. Relationship between K_g and E_K.

fracturing permeability was 2.61 times greater than K_g. The minimum E_K value was 0.43, corresponding to a 1.43-fold increase over K_g.

As shown in Fig. 10, the curve exhibits an arch-shaped trend, indicating that the effect of viscosity on flow capacity is nonlinear and complex. The experiments conducted with fluids of different viscosities used cores with comparable permeability, as verified by the data points enclosed in the dashed box in Fig. 1. Thus, the observed variations in permeability with viscosity are credible, suggesting the presence of an optimal viscosity rather than a simple monotonic relationship. With increasing viscosity, the injected fluid experiences stronger capillary resistance before the onset of core fracturing, leading to a higher P_f. However, after fracturing, the elevated viscosity causes reduced flow rates, thereby lowering the overall flow capacity compared with the previous data point. Before the viscosity reaches 19 mPa·s, E_K shows a steady increase, attaining a maximum value of 0.96, which corresponds to a 1.96-fold improvement in permeability. The enhancement factor decreases slightly thereafter, yielding values of 1.82 just below and 1.80 above 19 mPa·s. Therefore, in practical applications, it is essential to optimize fluid viscosity to achieve the best balance between economic cost and production efficiency.

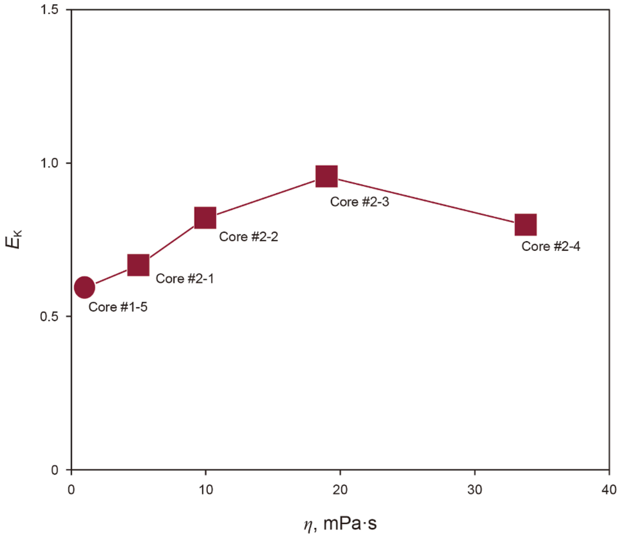

Fig. 10. Relationship between η and E_K. The data points in the figure correspond to the core numbers listed in Table 5 according to their viscosities.

3.2. Fracture propagation

The application of fracturing flooding technology effectively reverses the conventional approach of fluid loss prevention, instead promoting fluid loss. The significant loss of FFFs can substantially elevate pore pressure, facilitating the formation of micro fractures. Viscosity strongly influences the amount of fluid loss, which in turn affects the fracturing capability of the fluid. Therefore, it is crucial to compare the effects of different viscosities on fracture morphology under identical injection flow rate conditions. CT scanning has been demonstrated as an effective method for core physical experiments, as supported by extensive research (Fang et al., 2020; Jing et al., 2022; Li et al., 2021, 2023). Based on CT scanning, images of cores #2-1 to #2-4 were obtained following fracturing flooding. The 3D images in the vertical direction were constructed by stacking 1011 2D images. Fig. 11 presents the 250th, 500th, and 750th slices of the four cores, along with the images obtained prior to fracturing flooding.

It was observed that all cores exhibited some degree of fracturing after fracturing flooding, with core #2-3 showing significantly larger fracture apertures than the others. The presence of larger mineral grains and weaker cementation in core #2-3 likely caused fractures to form along the edges of the mineral grains, indicating that the particles were difficult to hold together under high fluid pressure. This observation also corroborates the previous analysis, as the E_K of core #2-3 reached its maximum due to a substantial fracture extending at least 2.5 cm.

In addition to core #2-3, the remaining three cores displayed minor fractures with distinct morphologies. In core #2-1, the fracture in the 250th slice extends along the edge with some missing portions, while the 750th slice shows a fracture traversing the core parallel to the bright mineral layer. Core #2-2 exhibits a small slanting cut fracture at a corner. Core #2-4 presents short-span splitting fractures extending nearly vertically from the surface into the core, indicating the strong fracturing effect of high-viscosity FFFs. These findings confirm that viscosity has a significant influence on fracture morphology and permeability enhancement in low-permeability sandstone reservoirs.

3.3. EOR performance

The impact of fracturing flooding on the recovery efficiency of low-permeability cores was examined using NMR (Liu and Sheng, 2020; Lu et al., 2022; Zhou et al., 2024). By measuring the T_2 spectra of cores under four conditions: water saturation, oil saturation, after conventional water flooding, and after fracturing flooding, we compared the retained crude oil volumes in pores under different displacement processes and evaluated the effects of various FFF types on residual oil distribution across different pore sizes. This approach allowed us to identify the pore size range mobilized by fracturing flooding and to evaluate the extent of recovery enhancement it provides. For high-water-cut reservoirs, the findings demonstrate the feasibility of employing fracturing flooding to improve recovery from a mechanistic standpoint and offer insights for reservoir development strategies. The properties of the cores and oil utilized in the experiments are detailed in Section 2.1. It is worth noting that the cores in Set #3 were free of fractures, as their permeabilities are comparable to those in Set #2, whose CT images (Fig. 11, original slice) confirm an absence of fractures.

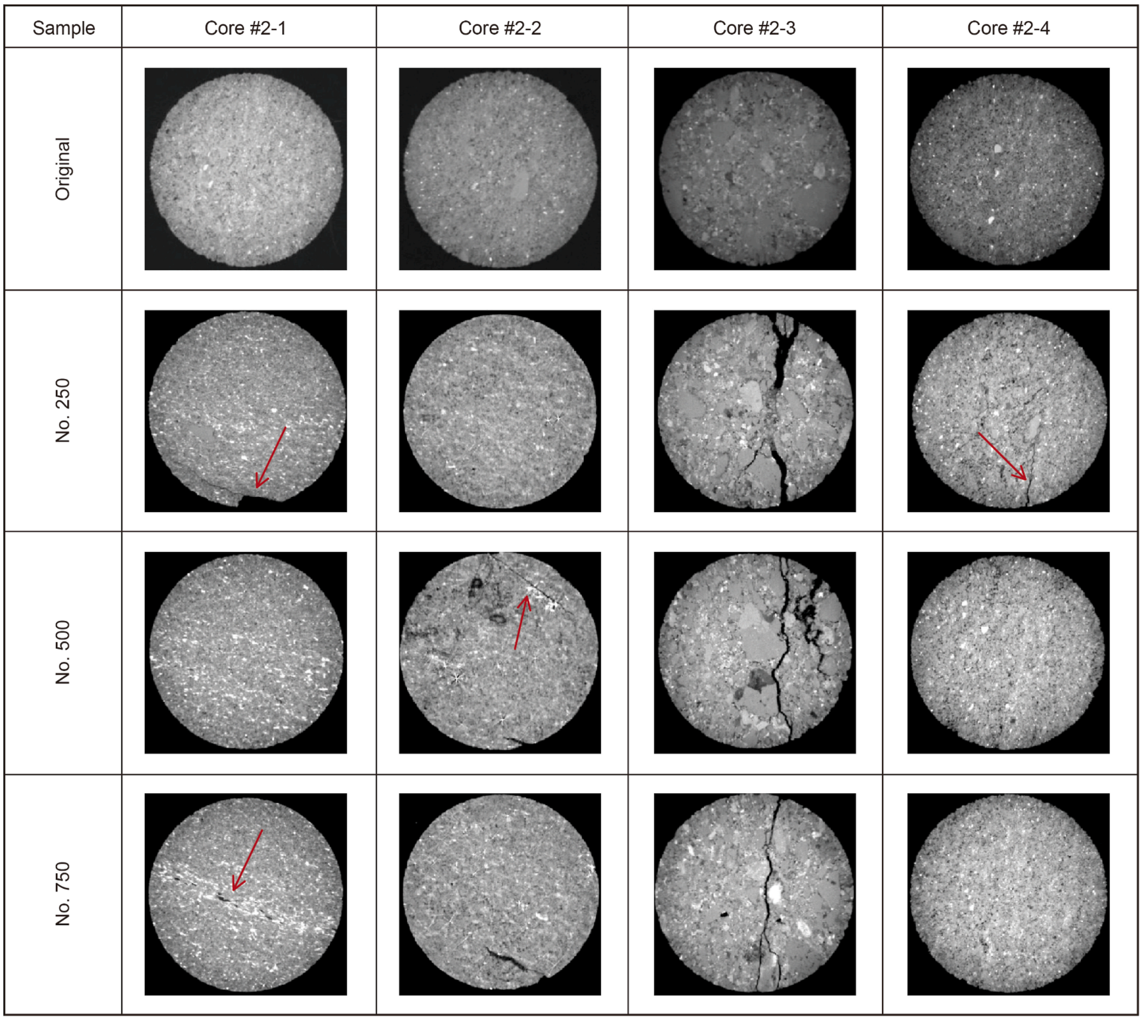

Fig. 11. 2D slice CT images of cores from Set #2.

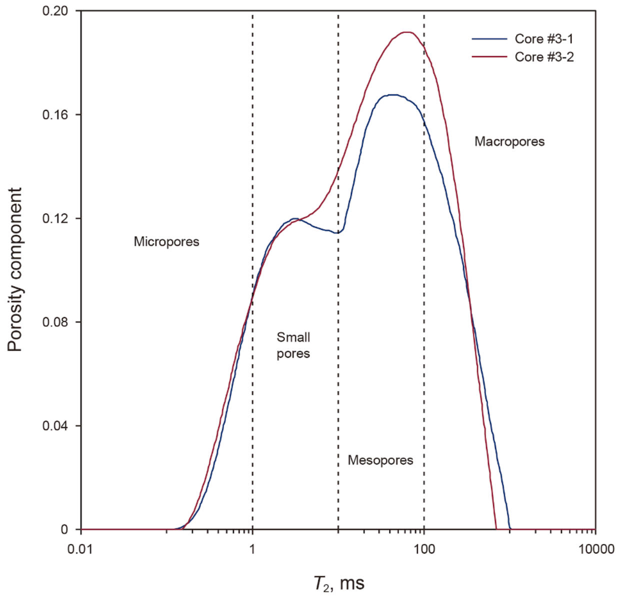

Fig. 12. T_2 spectrum after water saturation.

3.3.1. *Saturated water*

Fig. 12 illustrates the distribution of water within the pore spaces of the cores when they are fully saturated with water. The T_2 spectra exhibit a bimodal pattern, indicating that the pore structure of the cores is complex and comprises two or more distinct pore types (or pore size ranges). Comparison with multiple studies of pore classification (Liu et al., 2024; Lv et al., 2024; Wan et al., 2024) reveals the presence of four distinct pore types, each corresponding to a specific T_2 range, as summarized in Table 6.

As shown in Fig. 12, the bimodal T_2 distributions of cores #3-1 and #3-2 align well with the defined intervals, confirming the rationality of this classification. It should be noted that the vertical axis of the T_2 spectrum represents the porosity component, which is defined as the ratio of the pore volume occupied by hydrogen-containing fluids within a specific pore size range corresponding

Table 6
The classification of pore sizes corresponding T_2 values.

T_2, ms	Pore type	Pore radius, μm
≤1	Micropores	≤2
1–10	Small pores	2–10
10–100	Mesopores	10–20
≥100	Macropores	≥20

to a given T_2 value to the apparent bulk volume of the rock. The porosity component values were directly obtained from the NMR software without any post-processing or additional treatment.

3.3.2. Saturated oil

Figs. 13 and 14 respectively depict the T_2 spectra of cores #3-1 and #3-2 under water-saturated and oil-saturated conditions, exhibiting similar overall patterns. To differentiate the hydrogen signals of oil and water, each core was thoroughly flushed with a 20% $MnCl_2$ solution, which effectively suppressed the hydrogen signal originating from water. Consequently, the orange line represents the distribution of oil within the pore space, delineating pore size variations under the oil-saturated condition. This distribution directly reflects the mobility and spatial distribution of the movable fluid within the core.

The region between the red and orange curves represents the distribution of irreducible water. In the oil-saturated state, the T_2 spectrum displays a single-peak characteristic, with T_2 peak values exceeding 100 ms, indicating that oil predominantly resides within macropores and mesopores. This occurs because fluids in larger pores are less influenced by the solid skeleton, allowing for greater mobility under the same external pressure conditions. The relatively larger area between the red and orange curves in the micro, small, and mesopore regions and the smaller area in the macropore region indicate that irreducible water mainly occupies smaller pores and adheres to the walls of larger pores. The behavior of this irreducible water is heavily constrained by the rock framework and strong capillary forces, which bind it tightly and hinder its movement.

The disappearance of the left-hand peak in the orange curve (relative to the red one) and the rightward shift of the remaining peak, consistent with the displacement of saturated water by oil, indicate that oil preferentially invades macropores and mesopores. The hydrophilic nature of low-permeability sandstone generates strong capillary forces within micropores and small pores, which hinder oil entry, especially in narrow throats and blind pores. Nevertheless, a portion of oil remains distributed in these smaller pores, as the imposed displacement pressure enables oil to overcome capillary resistance. Moreover, the 24-h isothermal ageing process following displacement allows deeper oil penetration, leading to partial filling of micropores and small pores.

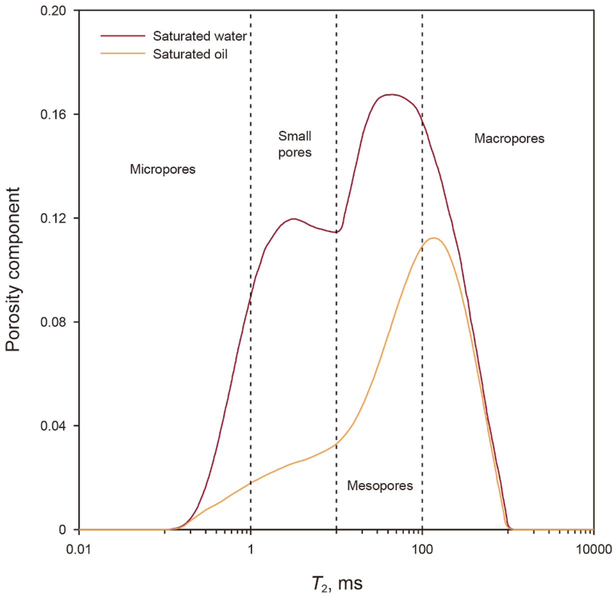

Fig. 13. T_2 spectrum of core #3-1 after saturated oil.

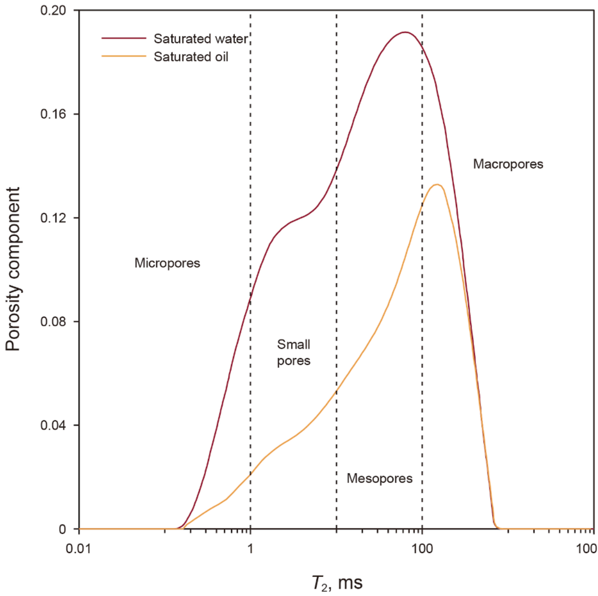

Fig. 14. T_2 spectrum of core #3-2 after saturated oil.

The enhancement of oil distribution in mesopores is particularly evident in core #3-1, where the orange curve transitions sharply from a gentle slope near the micro-mesopore boundary. This indicates that in low-permeability sandstones with pore radii greater than 10 μm, the inhibitory effect of capillary forces diminishes, facilitating oil entry into larger pores. Comparing the pre-peak trends of the orange curves between core #3-1 and core #3-2 reveals that the former displays a distinct inflection point, whereas the latter rises exponentially. This suggests that core #3-1 possesses a higher proportion of interconnected mesopores, while core #3-2 exhibits a more balanced connectivity between mesopores and small pores.

3.3.3. Water fracturing flooding

Core #3-1 was used to conduct water fracturing flooding. Before this process, the core that had been previously saturated with oil was subjected to conventional water flooding to shield the hydrogen signals. After completing the conventional water flooding, a third NMR test was performed to determine the residual oil distribution following this flooding (illustrated by the green line in Fig. 15). This stage corresponds to the high-water-cut stage in oilfield development.

At this stage, the T_2 spectrum (green line) shows a significant reduction compared to the saturated oil stage (orange line), particularly in mesopores and macropores. This indicates that conventional water flooding effectively removes crude oil from these larger pore systems. However, in smaller mesopores, small pores, and micropores, the overall downward shift of the green line relative to the orange line is less pronounced, implying lower recovery efficiency, consistent with field observations. The leftward and downward shift of the green line relative to the orange peak further confirms that mesopores and macropores exhibit higher oil recovery efficiency.

Combining the T_2 patterns during water flooding with the hydrophilic characteristics of low-permeability sandstone reservoirs yields two key insights:

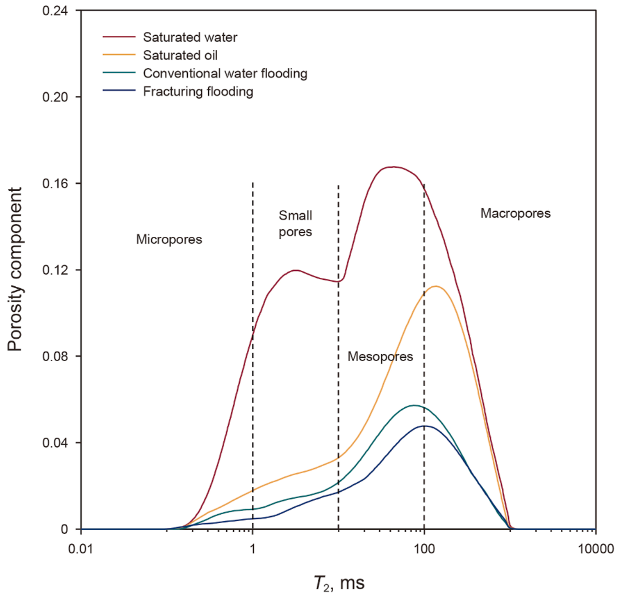

Fig. 15. T_2 spectrum of core #3-1 after fracturing flooding.

(1) In mesopores and macropores, two phase displacement (oil displacing water or water displacing oil) is primarily controlled by flow pressure, as both T_2 peaks fall within these pore ranges.
(2) The process is also influenced by wettability. Due to the hydrophilic nature of the sandstone, the T_2 peak of saturated oil after oil displacing water is located to the right of that corresponding to the saturated water stage, indicating that during reservoir formation, oil mainly occupies mesopores and macropores. In contrast, during late-stage water flooding, the T_2 peak shifts left, confirming that the water film improves oil displacement efficiency, with oil being expelled first from the larger pores.

During water fracturing flooding, a constant injection rate of 15 mL/min was applied to core #3-1 (the same as for core #3-2) to maintain flow pressure near P_f, the fracturing pressure. This choice is consistent with the parallel core experiments shown in Fig. 1, where core #1-5 fractured at a flow rate of 15 mL/min. The flooding continued until no oil was produced at the outlet. Afterwards, the system was left to stand for 24 h to simulate the soaking stage, ensuring sufficient oil–water displacement. Then, a constant-rate water flooding process was performed until oil production again ceased. The volumes of total fluid and oil produced were recorded, and NMR tests were conducted.

The resulting T_2 spectra represented four distinct stages for core #3-1:

(1) Before reservoir formation: 100% water saturation;
(2) After reservoir formation: S_{wc} (connate water saturation);
(3) Late development: high-water-cut stage;
(4) After fracturing flooding: S_{or} (residual oil saturation).

A comparison between the green and blue lines in Fig. 15 demonstrates that fracturing flooding significantly enhanced recovery efficiency in small pores and mesopores. The area enclosed by these lines in this pore size range provides qualitative evidence of consistent improvement in recovery. Moreover, a noticeable enhancement appears when T_2 = 100–200 ms (macropores of smaller size). Therefore, water fracturing flooding is proven to effectively improve oil recovery in small pores, mesopores, and certain macropores, as reflected by the overlapping segments of the green and blue curves in the T_2 spectra.

The calculation method for recovery efficiency based on NMR analysis is presented as follows:

$$R = \frac{\Delta A}{A_0} = \frac{A_0 - A_t}{A_0} \tag{6}$$

where R represents the recovery efficiency, dimensionless; A_0 denotes the area enclosed by the T_2 spectrum of the core saturated with oil and the X-axis (depicted by the orange line in Figs. 15 and 17), dimensionless; A_t is the area enclosed by the T_2 spectrum and the X-axis at different stages of reservoir development, dimensionless.

Accordingly, the formula for calculating recovery efficiency within different pore size ranges can be derived as follows:

$$R_i = \frac{\Delta A_i}{\Delta A}, i = 1, 2, 3, 4 \tag{7}$$

where R_i denotes the recovery efficiency for different pore sizes ($i = 1, 2, 3, 4$ corresponding to micropores, small pores, mesopores, and macropores, respectively), dimensionless; and A_i is the area enclosed by the T_2 spectrum for different pore sizes at two distinct reservoir stages, dimensionless.

Using Eqs. (6) and (7), the recovery efficiencies for conventional water flooding and water fracturing flooding were calculated from the T_2 spectra, with results illustrated in Fig. 16. A comparison across different pore sizes reveals a positive correlation between pore size and recovery efficiency, with larger pores corresponding to higher recovery efficiency. This trend holds for both conventional water flooding and fracturing flooding, as also confirmed by the recovery results of core #3-2 shown in Fig. 18.

A quantitative analysis of core #3-1 recovery data was carried out from two perspectives: (1) evaluating the oil recovery performance of different recovery methods across various pore types, and (2) conducting a comparative analysis between the two recovery methods within the same pore categories. This dual-angle assessment allowed for an objective evaluation of the applicability and quantitative performance indicators of different recovery techniques.

For conventional water flooding, the recovery efficiency increases with pore size, ranging from 20.41% in micropores to

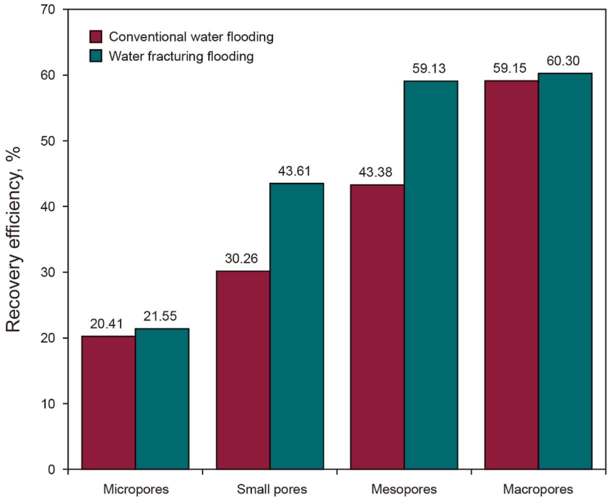

Fig. 16. Recovery efficiency of core #3-1.

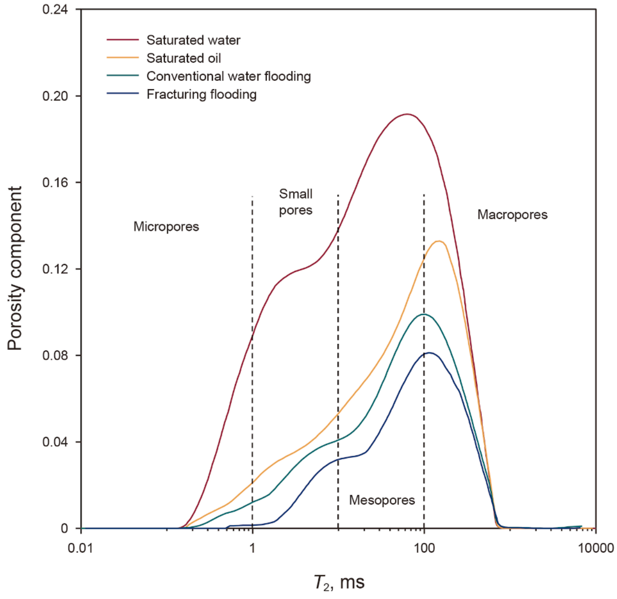

Fig. 17. T_2 spectrum of core #3-2 after fracturing flooding.

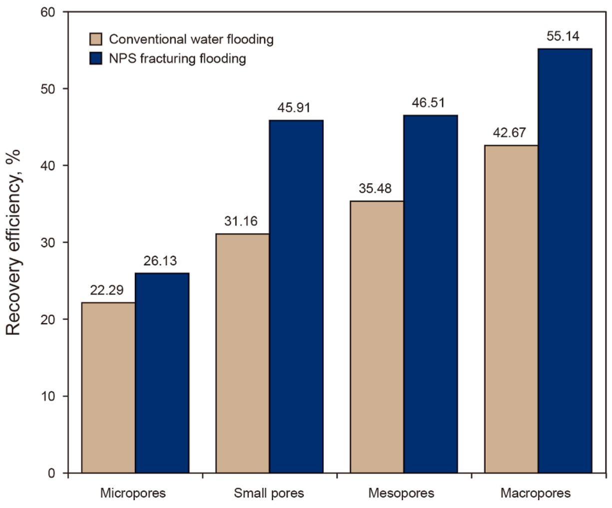

Fig. 18. Recovery efficiency of core #3-2.

59.15% in macropores. This phenomenon is a result of the combined effects of pressure gradient and rock wettability. As water enters the core from the high-pressure inlet face, its hydrophilic nature causes the oil to be displaced toward the outlet. The larger the pore, the more pronounced this displacement effect becomes. A similar pattern appears during formation water fracturing flooding, where recovery efficiency increases from 21.55% to 60.30%, reflecting a synergistic effect between pressure differential and wettability.

The data further reveal that fracturing flooding outperforms conventional water flooding across all pore sizes. Specifically, in micropores and macropores, recovery efficiency improves by approximately 1.2%, while in small pores and mesopores, the improvement exceeds 13%. This observation highlights a noteworthy phenomenon: extremely large or small pores tend to limit the effectiveness of formation water fracturing flooding, whereas moderate-sized pores (small pores and mesopores) exhibit marked enhancement under fracturing conditions. These pores, therefore, are most favorable for fracturing flooding.

Three main factors explain this pattern:

(1) In macropores, most oil is expelled during the conventional water flooding stage. The remaining residual oil, though limited in volume, cannot be mobilized even after fracturing flooding due to the stabilizing water film.
(2) Fracturing flooding generates new fracture networks within the core that serve as the dominant flow channels. As a result, a substantial portion of the driving pressure is dissipated along these fractures, leaving only a small amount of water able to penetrate the matrix pores. This limits any further improvements in efficiency.
(3) During the soaking stage, water can displace oil within mesopores and small pores, but small pores remain largely unaffected owing to the lack of sufficient driving force.

The integrated experimental sequence, which involves subjecting core #3-1 to conventional water flooding followed by fracturing flooding after reaching the high-water-cut stage, closely mirrors the oilfield development process. As a result, these findings provide valuable insights for improving oil recovery efficiency and guiding strategies for field-scale reservoir development.

3.3.4. NPS fracturing flooding

An NPS fracturing flooding experiment was performed on core #3-2. Similar to core #3-1, this core was first subjected to conventional water flooding prior to the implementation of fracturing flooding. Upon completion of the conventional water flooding, the residual oil T_2 spectrum was obtained using NMR, after which the NPS fracturing flooding procedure commenced. The displacement process was sustained under pressure for 24 h to simulate the soaking stage, followed by continuous water flooding and a final NMR measurement to determine the residual oil distribution.

The T_2 spectra corresponding to the four experimental stages for core #3-2 are illustrated in Fig. 17. After conventional water flooding, the residual oil T_2 peak (green line) shifted leftward relative to the orange line (saturated oil stage). Following the fracturing flooding, the residual oil T_2 (blue line) shifted rightward compared with the green line. This pattern closely resembles that observed for core #3-1, thereby confirming the consistency and reliability of the analytical interpretation made for that core.

A comparison of the orange and green lines reveals that conventional water flooding in core #3-2 effectively mobilized oil in the macropores. Specifically, within the $T_2 > 100$ ms range, the green line shows significantly lower amplitudes than the orange line. This can be attributed to the low interfacial tension of the NPS solution, which modifies the oil–water wettability and allows for the displacement of water-locked oil droplets within the macropores. In contrast, for T_2 values below 100 ms, the displacement effect of conventional water flooding is comparatively modest.

A comparison between the green and blue lines shows that, in the micropore, small pore, and mesopore regions, the blue line is significantly lower than the green line. This indicates that a larger volume of oil was mobilized and displaced after fracturing flooding, which is the desired outcome of this process.

Interestingly, the left peak of the green and blue curves reappears in contrast to the observations for core #3-1. This phenomenon suggests that during subsequent displacement, a smaller quantity of oil was produced, whereas a larger proportion of residual oil remained trapped within the fine pores. The increased signal amplitude in this region leads to a rise in the curve and the formation of a distinct peak, highlighting the heterogeneous redistribution of residual oil following NPS fracturing flooding.

The recovery efficiency bar chart for core #3-2 was calculated and is presented in Fig. 18. The analysis of recovery efficiency was carried out from two perspectives.

Firstly, it was observed that recovery efficiency increases with pore size, regardless of whether the displacement process involved conventional water flooding or NPS fracturing flooding. This trend is consistent with the observations made in core #3-1. However, in contrast to core #3-1, NPS fracturing flooding raised the minimum recovery efficiency (corresponding to micropores) to 26.13%, compared with 22.29% for conventional water flooding. The maximum recovery efficiency (upper limit) reached 55.14% under NPS fracturing flooding and 42.67% under conventional water flooding.

It is important to emphasize that improving recovery efficiency in small pores remains particularly challenging, highlighting the critical role of micropores, areas most impacted by low permeability and strong wettability, in optimizing the overall recovery performance of NPS fracturing flooding. The reduction in interfacial tension induced by NPS mitigates the Jamin effect within micropores, thereby promoting more effective oil–water displacement. Additionally, the degree of oil–water miscibility is enhanced, facilitating smoother displacement dynamics within these confined spaces.

When compared with conventional water flooding, NPS fracturing flooding demonstrates superior EOR performance across the entire pore-size spectrum. Specifically, the recovery efficiency achieved with NPS is 3.84%, 14.75%, 11.03%, and 12.47% higher than that of conventional water flooding in micropores, small pores, mesopores, and macropores, respectively.

The superior performance of NPS fracturing flooding, relative to core #3-1, can be attributed to its dual mechanisms:

(1) The ability of NPS to reduce interfacial tension, enabling greater mobilization of trapped oil within micropores.
(2) The fracturing flooding process, which enhances permeability and improves pore connectivity, allowing oil from previously isolated or blind-end pores to be mobilized.

These combined effects result in a marked improvement in displacement efficiency and overall oil recovery within low-permeability sandstone reservoirs.

The differences in pore structures between the cores indicate that, although cores #3-1 and #3-2 were obtained from the same formation and exhibit similar K_g, their ultimate recovery efficiencies may still vary. This variability is inherent to porous media. Therefore, when comparing water fracturing flooding with NPS fracturing flooding, it is inappropriate to directly compare recovery efficiencies. Instead, a recovery enhancement factor (E_R) is introduced to quantitatively describe the influence of different FFFs on recovery performance.

$$E_R = \frac{R_2 - R_1}{R_1} \tag{8}$$

where E_R denotes the recovery enhancement factor, dimensionless; while R_1 and R_2 represent the recovery efficiency of conventional water flooding and FFF fracturing flooding, respectively, both dimensionless.

As illustrated in Fig. 19, NPS fracturing flooding exhibits superior performance in displacing and replacing oil within both micropores and macropores compared to water fracturing flooding. Specifically, the recovery E_R of NPS fracturing flooding is approximately 15 times higher than that of water fracturing flooding in macropores, and about 3 times higher than in micropores, primarily due to the reduction in oil–water interfacial tension by NPS. In small pores and mesopores, the effects of NPS and water fracturing flooding are comparable, yet both are more pronounced than those observed in micropores and macropores.

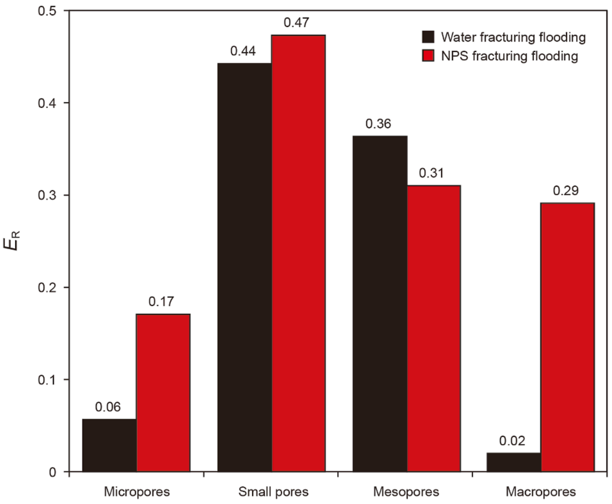

Fig. 19. E_R of water fracturing flooding and NPS fracturing flooding.

The analysis of core #3-1 indicates that small pores and mesopores are the dominant sites of oil–water displacement during the 24-h simulated soaking stage. In contrast, oil trapped within micropores and oil blocked by water films in macropores exhibit limited mobility. The reduced interfacial tension of NPS compared with water contributes to higher recovery efficiency in micropores after NPS fracturing flooding, though still lower than that in small pores and mesopores.

Overall, the following general understanding can be derived regarding the mechanism by which fracturing flooding improves recovery efficiency: water fracturing flooding is most effective in mobilizing residual oil within small pores and mesopores, whereas NPS fracturing flooding can mobilize residual oil across the full pore size distribution. Consequently, the overall performance of NPS fracturing flooding surpasses that of water fracturing flooding. Nevertheless, considering the balance among chemical agent costs (e.g., NPS or other surfactants), the energy consumption associated with driving pressure, and the practical production benefits, prudent implementation strategies are essential in oilfield development.

4. Conclusions

This study investigated the fracture pressure (P_f) and EOR mechanisms of low-permeability sandstone reservoirs during the high-water-cut stage through fracturing flooding experiments integrated with CT scanning and NMR analysis. The experiments examined P_f under varying N_2 permeability (K_g) and fracturing-flooding fluid (FFF) viscosities, elucidated the mechanisms of flow capacity improvement, and used CT imaging to characterize fracture morphology. NMR measurements were further employed to evaluate the EOR performance of fracturing flooding. The main conclusions are as follows:

(1) Fracture pressure behavior: P_f exhibits an exponentially decreasing relationship with K_g. As K_g decreases, P_f increases rapidly. Moreover, P_f increases logarithmically with increasing FFF viscosity, although the growth rate gradually diminishes, suggesting that both formation conditions and

economic factors should be considered to determine the optimal viscosity.

(2) Energy efficiency and fracture effectiveness: The energy E_K decreases with increasing K_g, ranging from a maximum of 1.61 to a minimum of 0.43. With increasing FFF viscosity, E_K first rises and then declines, reaching a peak value of 0.96 at a viscosity of 19 mPa·s. Beyond this point, stimulation effectiveness deteriorates, as confirmed by two-dimensional CT slice analysis.

(3) EOR performance and pore-scale behavior: The type of FFF strongly affects oil recovery. Compared with conventional water flooding, water fracturing flooding enhances residual oil mobilization in small pores and mesopores, increasing recovery from 30.26% and 43.38% to 43.61% and 59.13%, respectively. NPS fracturing flooding exhibits superior sweep efficiency across the full pore-size range, particularly in micropores and macropores where water fracturing flooding is less effective, elevating recovery from 22.29% and 42.47% to 26.13% and 55.14%, respectively.

This study provides new theoretical insights into the EOR mechanisms of fracturing flooding in low-permeability sandstone reservoirs during the high-water-cut stage. Nevertheless, limitations still exist, particularly the lack of in-situ CT imaging for real-time observation of fracture propagation. Future work will incorporate full-diameter core experiments combined with in-situ CT scanning to further elucidate fracture propagation mechanisms.

CRediT authorship contribution statement

Lei Zhang: Writing – review & editing, Supervision, Project administration, Methodology, Conceptualization. **Hua-Peng Jing:** Writing – original draft, Visualization, Validation, Methodology, Data curation. **Li-Yuan Dong:** Visualization, Validation, Methodology. **Gloire Imani:** Writing – review & editing. **Dong-Yan Fan:** Project administration, Funding acquisition, Data curation. **Shuai-Shi Fu:** Validation, Supervision, Formal analysis. **Bilal Shams Memon:** Visualization, Resources, Formal analysis. **Yong-Fei Yang:** Writing – review & editing, Methodology, Conceptualization. **Jun Yao:** Writing – review & editing, Methodology, Funding acquisition, Conceptualization. **Hai Sun:** Writing – review & editing, Resources, Funding acquisition, Conceptualization.

Declaration of competing interest

The authors declare that they have no known competing financial interests or personal relationships that could have appeared to influence the work reported in this paper.

Acknowledgements

We would like to express appreciation to the financial support from the Oil & Gas Major Project (No. 2025ZD1404401), the National Natural Science Foundation of China (Grant Nos. U24B6001, 42090024, 42377138, and 52034010), Shandong Provincial Natural Science Foundation (Grant Nos. ZR2022JQ23 and ZR2025MS854), and the Fundamental Research Funds for the Central Universities (Grant No. 25CX02004A).

References

Aljawad, M.S., Aljulaih, H., Mahmoud, M., et al., 2019. Integration of field, laboratory, and modeling aspects of acid fracturing: A comprehensive review. J. Petrol. Sci. Eng. 181, 106158. https://doi.org/10.1016/j.petrol.2019.06.022.

Bai, B., Zhu, R.K., Wu, S.T., et al., 2013. Multi-scale method of nano (micro)-CT study on microscopic pore structure of tight sandstone of Yanchang Formation, Ordos Basin. Petrol. Explor. Dev. 40 (3), 354–358. https://doi.org/10.1016/S1876-3804(13)60042-7.

Bai, L.H., Liu, B., Chi, Y.A., et al., 2021. 2D NMR studies of fluids in organic-rich shale from the Qingshankou Formation, Songliao Basin. Oil Gas Geol. 42 (6), 1389–1400. http://ogg.pepris.com/CN/10.11743/ogg20210613 (in Chinese).

Bennour, Z., Ishida, T., Nagaya, Y., et al., 2015. Crack extension in hydraulic fracturing of shale cores using viscous oil, water, and liquid carbon dioxide. Rock Mech. Rock Eng. 48, 1463–1473. https://doi.org/10.1007/s00603-015-0774-2.

Chen, X., Li, Y.Q., Liu, Z.Y., et al., 2023. Experimental investigation on the enhanced oil recovery efficiency of polymeric surfactant: Matching relationship with core and emulsification ability. Pet. Sci. 20 (1), 619–635. https://doi.org/10.1016/j.petsci.2022.11.002.

Cheng, Z.L., Wang, Q., Ning, Z.F., et al., 2018. Effect of boundary conditions on spontaneous imbibition in oil-water and gas-water systems for tight sandstone using NMR. Petrol. Sci. Bull. 3 (3), 272–283. https://www.cup.edu.cn/sykxtb/gkll/2018/vol3/issue33/166252.htm (in Chinese).

Cnudde, V., Boone, M., Dewanckele, J., et al., 2011. 3D characterization of sandstone by means of X-ray computed tomography. Geosphere 7 (1), 54–61. https://doi.org/10.1130/GES00563.1.

Dai, Y.X., Zhang, X.L., Liu, S.Y., et al., 2024. Syntheses and properties of associative acrylamide copolymers containing short hydrophobic chains used in a friction reducer for slick-water fracturing. Pet. Sci. 21 (3), 1889–1901. https://doi.org/10.1016/j.petsci.2024.03.013.

Ding, M.C., Xue, X.F., Wang, Y.F., et al., 2024. Mobilization of tight oil by spontaneous imbibition of surfactants. Pet. Sci. 21 (6), 4176–4188. https://doi.org/10.1016/j.petsci.2024.08.010.

Fang, H.H., Sang, S.X., Liu, S.Q., 2020. Three-dimensional spatial structure of the macro-pores and flow simulation in anthracite coal based on X-ray μ-CT scanning data. Pet. Sci. 17, 1221–1236. https://doi.org/10.1007/s12182-020-00485-3.

Feng, X.T., Chen, S.L., Zhou, H., 2004. Real-time computerized tomography (CT) experiments on sandstone damage evolution during triaxial compression with chemical corrosion. Int. J. Rock Mech. Min. Sci. 41 (2), 181–192. https://doi.org/10.1016/S1365-1609(03)00059-5.

Gao, H., Wang, C., Cao, J., et al., 2019. Quantitative study on the stress sensitivity of pores in tight sandstone reservoirs of Ordos basin using NMR technique. J. Petrol. Sci. Eng. 172, 401–410. https://doi.org/10.1016/j.petrol.2018.09.08.

Guo, J.C., Zhou, H.Y., Zeng, J., et al., 2020. Advances in low-field nuclear magnetic resonance (NMR) technologies applied for characterization of pore space inside rocks: A critical review. Pet. Sci. 17, 1281–1297. https://doi.org/10.1007/s12182-020-00488-0.

Guo, T.K., Tang, S.J., Liu, S., et al., 2021. Physical simulation of hydraulic fracturing of large-sized tight sandstone outcrops. SPE J. 26 (1), 372–393. https://doi.org/10.2118/204210-PA.

He, J.G., Wang, H.W., 2018. Design and effect of fracture-flooding in class III oil reservoirs. J. Southwest Petrol. Univ. Sci. Technol. Edit. 40 (5), 95–104. http://www.xml-data.org/XNSYDXXBZRB/HTML/2018-5-95.htm (in Chinese).

Jia, C.Z., Zheng, M., Zhang, Y.F., 2012. Unconventional hydrocarbon resources in China and the prospect of exploration and development. Petrol. Explor. Dev. 39 (2), 129–136. https://doi.org/10.1016/S1876-3804(12)60026-3.

Jiang, N., Zhang, Z., Qu, G.H., et al., 2022. Distribution characteristics of micro remaining oil of class III reservoirs after fracture flooding in Daqing Oilfield. Energies 15 (9), 3385. https://doi.org/10.3390/en15093385.

Jiang, Y.L., Liang, W.G., Lian, H.J., et al., 2025. Experimental study of hydraulic fracture propagation in multi-hole synchronous fracturing in horizontal wells in sandstone. Int. J. Rock Mech. Min. Sci. 186, 106013. https://doi.org/10.1016/j.ijrmms.2024.106013.

Jing, W.L., Zhang, L., Li, A.F., et al., 2022. Investigation of pore-scale remaining oil dynamic evolution in heterogeneous marine carbonate using real-time computed tomography scanning. Energy Fuels. 36 (15), 8180–8188. https://doi.org/10.1021/acs.energyfuels.2c01497.

Jing, W.L., Zhang, L., Li, A.F., et al., 2024. Phase behaviors of gas condensate at pore scale: Direct visualization via microfluidics and in-situ CT scanning. SPE J. 29 (5), 2566–2577. https://doi.org/10.2118/218421-PA.

Ju, Y., Guo, F., Zhang, G.L., et al., 2025. Effects of high temperatures and horizontal geostress differences on hydraulic fracture propagation in tight sandstones: An experimental investigation. Geoenergy Sci. Eng. 246, 213644. https://doi.org/10.1016/j.geoen.2025.213644.

Lai, J., Wang, G.W., Fan, Z.Y., et al., 2016. Insight into the pore structure of tight sandstones using NMR and HPMI measurements. Energy Fuels 30 (12), 10200–10214. https://doi.org/10.1021/acs.energyfuels.6b01982.

Li, J., Li, X.R., Song, M.S., et al., 2021. Investigating microscopic seepage characteristics and fracture effectiveness of tight sandstones: A digital core approach. Pet. Sci. 18, 173–182. https://doi.org/10.1007/s12182-020-00464-8.

Li, Q.G., Lin, B.Q., Zhai, C., et al., 2013. Experimental study on action characteristic of pulsating parameters incoal seam pulse hydraulic fracturing. J. China Coal Soc. 38 (7), 1185–1190. https://link.cnki.net/doi/10.13225/j.cnki.jccs.2013.07.027 (in Chinese).

Li, Y.W., Yang, S., Zhao, W.C., et al., 2018. Experimental of hydraulic fracture propagation using fixed-point multistage fracturing in a vertical well in tight sandstone reservoir. J. Petrol. Sci. Eng. 171, 704–713. https://doi.org/10.1016/j.petrol.2018.07.080.

Li, Z.H., Yun, Q.Q., Tang, W.J., et al., 2023. Phase behavior of petroleum sulfonate and the effect of its emulsification on enhanced oil recovery. Oilfield Chem. 37 (3), 468–473. https://ythx.scu.edu.cn/ythxen/article/abstract/20200316 (in Chinese).

Lian, P.Q., Gao, W.B., Tang, X., et al., 2020. Workflow for pore-type classification of carbonate reservoirs based on CT scanned images. Oil Gas Geol. 41 (4), 852–861. http://ogg.pepris.com/EN/abstract/abstract12050.shtml (in Chinese).

Liao, G.Z., Wang, Q., Wang, H.Z., et al., 2017. Chemical flooding development status and prospect. Acta Pet. Sin. 38 (2), 196. https://www.syxb-cps.com.cn/EN/Y2017/V38/I2/196 (in Chinese).

Liu, J.L., Xie, R.H., Guo, J.F., et al., 2024. Study of nuclear magnetic resonance response mechanism in shale oil and correction of petrophysical parameters. Fuel 358, 130162. https://doi.org/10.1016/j.fuel.2023.130162.

Liu, J.R., Sheng, J.J., 2020. Investigation of countercurrent imbibition in oil-wet tight cores using NMR technology. SPE J. 25 (5), 2601–2614. https://doi.org/10.2118/201099-PA.

Liu, N.Z., Zou, Y.S., Ma, X.F., et al., 2019. Study of hydraulic fracture growth behavior in heterogeneous tight sandstone formations using CT scanning and acoustic emission monitoring. Pet. Sci. 16, 396–408. https://doi.org/10.1007/s12182-018-0290-6.

Liu, Q., Sun, M.D., Sun, X.D., et al., 2023. Pore network characterization of shale reservoirs through state-of-the-art X-ray computed tomography: A review. Gas Sci. Eng. 113, 204967. https://doi.org/10.1016/j.jgsce.2023.204967.

Liu, X.F., Wang, J.F., Ge, L., et al., 2017. Pore-scale characterization of tight sandstone in Yanchang Formation Ordos Basin China using micro-CT and SEM imaging from nm-to cm-scale. Fuel 209, 254–264. https://doi.org/10.1016/j.fuel.2017.07.068.

Liu, Y.K., Wang, F.J., Wang, Y.M., et al., 2022. The mechanism of hydraulic fracturing assisted oil displacement to enhance oil recovery in low and medium permeability reservoirs. Petrol. Explor. Dev. 49 (4), 864–873. https://doi.org/10.1016/S1876-3804(22)60316-1.

Lu, T.J., Zeng, K.C., Jiang, P.X., et al., 2022. Competitive adsorption in CO_2 enhancing shale gas: Low-field NMR measurement combined with molecular simulation for selectivity and displacement efficiency model. Chem. Eng. J. 440, 135865. https://doi.org/10.1016/j.cej.2022.135865.

Lv, W., Gong, H.J., Dong, M.Z., et al., 2024. Potential of nonionic polyether surfactant-assisted CO_2 huff-n-puff for enhanced oil recovery and CO_2 storage in ultra-low permeability unconventional reservoirs. Fuel 359, 130474. https://doi.org/10.1016/j.fuel.2023.130474.

Ma, D.D., Cheng, C.K., Ding, C.K., et al., 2021. Comparisons of fracturing mechanism of tight sandstone using liquid CO_2 and water. J. Nat. Gas Sci. Eng. 94, 104108. https://doi.org/10.1016/j.jngse.2021.10410.

Ma, T.S., Chen, P., 2014. Study of meso-damage characteristics of shale hydration based on CT scanning technology. Petrol. Explor. Dev. 41 (2), 249–256. https://doi.org/10.1016/S1876-3804(14)60029-X.

Ma, Z.Z., Wang, Y.B., Zheng, Y.K., 2022. *In situ* dynamic X-ray imaging of fluid-rock interactions inside tight sandstone during hydraulic fracturing: Fluid flow process and fracture network growth. J. Petrol. Sci. Eng. 214, 110490. https://doi.org/10.1016/j.petrol.2022.110490.

Mu, J.F., Gao, Z.L., Zhang, L., et al., 2021. Experimental study of the effect of water and liquid CO_2, fracturingon shale fracture morphology. Unconvent. Oil Gas 8 (5), 87–92. https://link.cnki.net/doi/10.19901/j.fcgyq.2021.05.12 (in Chinese).

Negin, C., Ali, S., Xie, Q., 2017. Most common surfactants employed in chemical enhanced oil recovery. Petroleum 3 (2), 197–211. https://doi.org/10.1016/j.petlm.2016.11.007.

Nguyen, T.T., Sulem, J., Muhammed, R.D., et al., 2022. An experimental setup with radial injection cell for investigation of fracturing in unconsolidated sand reservoirs under fluid injection. J. Petrol. Sci. Eng. 213, 110362. https://doi.org/10.1016/j.petrol.2022.110362.

Osiptsov, A.A., 2017. Fluid mechanics of hydraulic fracturing: A review. J. Petrol. Sci. Eng. 156, 513–535. https://doi.org/10.1016/j.petrol.2017.05.019.

Pan, H.J., Wei, C., Yan, X.F., et al., 2024. 3D rock physics template-based probabilistic estimation of tight sandstone reservoir properties. Pet. Sci. 21 (5), 3090–3101. https://doi.org/10.1016/j.petsci.2024.04.010.

Ren, Z.J., Shen, Y.X., Gao, H.M., et al., 2021. Comparison of sodium oleate and sodium petroleum sulfonate for low-temperature flotation of fluorite and the collecting mechanisms. Min. Metall. Explor. 38, 2527–2536. https://doi.org/10.1007/s42461-021-00494-9.

Seright, R.S., Wang, D.M., 2023. Polymer flooding: Current status and future directions. Pet. Sci. 20 (2), 910–921. https://doi.org/10.1016/j.petsci.2023.02.002.

She, C.Y., Peng, H., Yang, J., et al., 2023. Experimental study on the true triaxial fracturing of tight sandstone with supercritical CO_2 and slickwater. Geoenergy Sci. Eng. 228, 211977. https://doi.org/10.1016/j.geoen.2023.211977.

Shi, B.Z., Xia, B.R., Lin, Y.X., et al., 2012. CT imaging and mechanism analysis of crack development by hydration in hard-brittle shale formations. Acta Pet. Sin. 33 (1), 137. https://www.syxb-cps.com.cn/EN/Y2012/V33/I1/137 (in Chinese).

Shi, X.Y., Wen, G.J., Bai, J.H., et al., 2016. A physical simulation experiment on fracture propagation of coalpetrography in hydraulie fracturing. J. China Coal Soc. 41 (5), 1145–1151. https://link.cnki.net/doi/10.13225/j.cnki.jccs.2015.0904 (in Chinese).

Sun, Q., Zhang, Y.F., Yu, C.L., et al., 2024. Experimental study on fracture initiation and propagationcharacteristics caused by pressure drive inlow-permeability sandstone reservoirs. Petrol. Geol. Recov. Eff. 31 (6), 160–167. https://link.cnki.net/doi/10.13673/j.pgre.202307001 (in Chinese).

Sun, Q., Zhou, Z.H., Zhang, Q., et al., 2020. Effect of electrolyte on synergism for reducing interfacial tension between betaine and petroleum sulfonate. Energy Fuels 34 (3), 3188–3198. https://doi.org/10.1021/acs.energyfuels.0c00153.

Tiwari, P., Deo, M., Lin, C.L., et al., 2013. Characterization of oil shale pore structure before and after pyrolysis by using X-ray micro CT. Fuel 107, 547–554. https://doi.org/10.1016/j.fuel.2013.01.006.

Wan, T., Zhang, J., Wu, B.C., 2024. NMR and CT characterizing the influence of O_2 in air injection performance in shale oil cores. Fuel 356, 129639. https://doi.org/10.1016/j.fuel.2023.129639.

Wang, F.J., Xu, H., Liu, Y.K., et al., 2024. The mechanism of hydraulic fracturing-assisted oil displacement technique applied to enhance oil recovery by high-pressure reduced adsorption. Acta Pet. Sin. 45 (2), 403–411. https://www.syxb-cps.com.cn/EN/Y2024/V45/I2/403 (in Chinese).

Wang, F.Y., Yang, K., Zai, Y., 2020. Multifractal characteristics of shale and tight sandstone pore structures with nitrogen adsorption and nuclear magnetic resonance. Pet. Sci. 17, 1209–1220. https://doi.org/10.1007/s12182-020-00494-2.

Wang, H.M., Tao, L.Y., Wang, J.G., et al., 2025. Influence of surfactants on wettability alteration during hydraulic fracturing in sandstone reservoirs: NMR analysis in spontaneous imbibition experiments. Geoenergy Sci. Eng. 247, 213695. https://doi.org/10.1016/j.geoen.2025.213695.

Wang, H.T., Lun, Z.M., Lv, C.Y., et al., 2017. Nuclear-magnetic-resonance study on mechanisms of oil mobilization in tight sandstone reservoir exposed to carbon dioxide. SPE J. 23 (3), 750–761. https://doi.org/10.2118/179554-PA.

Wei, W., Cai, J.C., Xiao, J.F., et al., 2018. Kozeny-Carman constant of porous media: Insights from fractal-capillary imbibition theory. Fuel 234, 1373–1379. https://doi.org/10.1016/j.fuel.2018.08.012.

Yang, B., Huang, H., Ren, Q.Q., et al., 2025. Quantitative insight into fracture distribution during supercritical CO_2 fracturing on tight sandstone formation. Pet. Sci. 22 (4), 1670–1685. https://doi.org/10.1016/j.petsci.2025.02.006.

Yang, K., Wang, F.Y., Zhao, J.Y., 2023a. Experimental study of surfactant-enhanced spontaneous imbibition in fractured tight sandstone reservoirs: The effect of fracture distribution. Pet. Sci. 20 (1), 370–381. https://doi.org/10.1016/j.petsci.2022.09.033.

Yang, L., Sheng, X.C., Zhang, B., et al., 2023b. Propagation behavior of hydraulic fractures in shale under triaxial compression considering the influence of sandstone layers. Gas Sci. Eng. 110, 204895. https://doi.org/10.1016/j.jgsce.2023.204895.

Yang, Y., Zhang, S.M., Cao, X.P., et al., 2023c. Practice and understanding of pressure drive development technology for low-permeability reservoirs in Shengli Oilfield. Petrol. Geol. Recov. Eff. 30 (6), 61–71. http://yqdzycsl.cnjournals.com/pgreen/article/abstract/202306007 (in Chinese).

Yerramilli, R.C., Zitha, P.L.J., Yerramilli, S.S., et al., 2015. A novel water-injectivity model and experimental validation with CT-scanned corefloods. SPE J. 20 (6), 1200–1211. https://doi.org/10.2118/165194-PA.

Yin, X.D., Jiang, S., Chen, S.J., et al., 2020. Impact of rock type on the pore structures and physical properties within a tight sandstone reservoir in the Ordos Basin, NW China. Pet. Sci. 17, 896–911. https://doi.org/10.1007/s12182-020-00460-y.

Zang, Y.X., Wang, H.Z., Wang, B., et al., 2024. In-situ laboratory study on influencing factors of pre-SC-CO_2 hybrid fracturing effect in shale oil reservoirs. Pet. Sci. 21 (5), 3547–3557. https://doi.org/10.1016/j.petrol.2022.110490.

Zhai, C., Li, X.Z., Li, Q., Gui, 2011. Research and application of coal seam pulse hydraulie fracturing technology. J. China Coal Soc. 36 (12), 1996–2001. https://link.cnki.net/doi/10.13225/j.cnki.jccs.2011.12.010 (in Chinese).

Zhang, Y.F., Yang, Y., Sun, Z.G., et al., 2022. Physical simulation of fracturing-flooding and quantitative characterization of fractures in low-permeability oil reservoirs. Petrol. Geol. Recov. Eff. 29 (4), 143–149. http://yqdzycsl.cnjournals.com/pgreen/article/abstract/202204017 (in Chinese).

Zhong, X.Y., Zhu, Y.S., Liu, L.P., et al., 2020. The characteristics and influencing factors of permeability stress sensitivity of tight sandstone reservoirs. J. Petrol. Sci. Eng. 191, 107221. https://doi.org/10.1016/j.petrol.2020.107221.

Zhou, Z.L., Jia, H., Zhang, R., 2024. Novel methods for cost-effectively generating a heterogeneous core model based on scale change of nuclear magnetic resonance and X-ray computed tomography data. SPE J. 29 (10), 5410–5425. https://doi.org/10.2118/221490-PA.